Evaluation and Origin of Residual Stress in Hybrid Metal and Extrusion Bonding and Comparison with Friction Stir Welding

A. Tognan , L. Sandnes , G. Totis , M. Sortino , F. Berto , Ø. Grong , E. Salvati

PII: S0020-7403(22)00026-1
DOI: https://doi.org/10.1016/j.ijmecsci.2022.107089
Reference: MS 107089

To appear in: *International Journal of Mechanical Sciences*

Received date: 21 October 2021
Revised date: 22 December 2021
Accepted date: 13 January 2022

Please cite this article as: A. Tognan , L. Sandnes , G. Totis , M. Sortino , F. Berto , Ø. Grong , E. Salvati , Evaluation and Origin of Residual Stress in Hybrid Metal and Extrusion Bonding and Comparison with Friction Stir Welding, *International Journal of Mechanical Sciences* (2022), doi: https://doi.org/10.1016/j.ijmecsci.2022.107089

Highlights

- Residual stress in HYB was evaluated for the first time
- Residual stress in FSW was assessed for comparison with HYB
- HYB weld showed a higher magnitude of tensile residual stress than FSW
- Higher residual stress in HYB was attributed to the presence of a filler material
- HYB showed more joint transverse distortion as compared with FSW

Evaluation and Origin of Residual Stress in Hybrid Metal and Extrusion Bonding and Comparison with Friction Stir Welding

A. Tognan[1a], L. Sandnes[2], G. Totis[1], M. Sortino[1], F.Berto[2], Ø. Grong[2], E. Salvati[1a]

[1]Polytechnic Department of Engineering and Architecture (DPIA), University of Udine, Via delle Scienze 206, Udine, 33100, Italy

[2]Department of Mechanical and Industrial Engineering, Norwegian University of Science and Technology, Richard Birkelands vei 2b, 7491 Trondheim, Norway

[a]Corresponding authors' email: tognan.alessandro@spes.uniud.it (Alessandro Tognan), enrico.salvati@uniud.it (Enrico Salvati)

1 Abstract

Hybrid metal and extrusion bonding (HYB) is an emerging solid-state welding technique that was developed about ten years ago. HYB exploits the fundamental idea of the well-established friction stir welding (FSW) technology, but a filler material is employed to enhance control of the weld microstructure and mechanical properties of the joint. HYB and FSW allow joining to be performed at lower temperatures than classical fusion welding methods. Still, thermal gradient effects seem impossible to be entirely avoided, thus leading to residual stress within the weld region and neighbouring material. Although the FSW-induced residual stress evaluation has been extensively studied and understood, the evaluation and interpretation of HYB-induced residual stress have not been tackled so far. In the present paper, a quantitative investigation on residual stress and its origin in HYB was carried out for the first time. Specifically, a 4 mm thick AA6082-

T6 HYB and a 4 mm thick AA6082-T6 FSW butt welds were considered. For the particular case of HYB, an AA6082-T4 was used as the filler material. In both cases, the full-field longitudinal residual stress was experimentally assessed using the Contour Method. The results showed that the HYB joint yields a higher magnitude of tensile residual stress compared to that of the FSW counterpart. A physical explanation for this difference in magnitude was attributed to the lower yield stress point exhibited by the filler material. Furthermore, the analysis revealed peak values of residual stress as high as 205±25 MPa and 165±15 MPa, for the HYB and FSW joint, respectively. Despite this, a similar distribution of residual stress across the weld was observed in both cases. An additional qualitative analysis on the transverse distortion of the welds outlined a pronounced undesired "V-like" deformation of the HYB joint of approximately 1.4°. By contrast, the FSW joint seemed not to show any perceptible bend.

Keywords Hybrid Metal and Extrusion Bonding, Friction Stir Welding, Residual Stress, Contour Method, Aluminium Alloy

2 Introduction

Solid-state welding refers to a broad class of welding techniques in which workpieces are joined below the melting point of the base material (BM) being welded. Solid-state welding techniques have been developed to overcome the main limitations affecting the traditional fusion welding. Because there is no material melting involved in solid-state welding, the thermal input is significantly lower than that of fusion welding, and the extent of heat-affected zone softening is reduced. Consequently, fewer microstructural changes occur within this softened zone, and the overall structural performance of the joint is typically improved. Solid-state welding also allows for joining both similar and dissimilar materials that are often considered difficult to fusion weld [1].

Amongst the family of solid-state welding, friction stir welding (FSW) has been particularly attracting attention in the last decades. This solid-state welding method was developed by The Welding Institute (TWI) of the UK in 1991. Basically, this technique employs a non-consumable rotating pin to join two facing workpieces (Fig. 1(a)), usually plates. Due to the contact of the rotating pin and the sides of the material undergoing welding, a source of heat is generated by friction. As a consequence, the BM undergoes local softening and plastic deformations, which eventually facilitate the two sides to merge together. As the pin travels along the weld direction, the material left behind experiences cooling until reaching room temperature. At this point, the welding process ends [2]. Throughout the years, FSW has evolved so that it can also handle joints in different configurations such as butt welds, T-butt and T-lap joints [2]–[4]. Many works in literature proved the capability of FSW to weld similar [5], [6] and dissimilar material pairs [7], [8]. Furthermore, FSW provides sound joints with limited defects and porosity [9]. Despite the significant advantages of FSW, it does not involve the use of any filler material (FM) which would provide a gradual transition between the BMs being welded in several aspects.

About ten years ago, the development of the hybrid metal and extrusion bonding (HYB) enabled to combine the advantages of the FSW with the use of FM. HYB relies on the processing

principle of FSW, see Fig. 1(b). However, continuous extrusion and injection of an aluminium FM into the weld groove is utilised to consolidate the joint [10]. Further studies showed the great potential of HYB to weld together up to three dissimilar BMs, plus the FM, and perform butt, slot and fillet welds. In addition, a set of equations were derived for tuning the HYB process parameters, such as FM feed rate, pin rotation speed and overall energy consumption [11]. Therefore, HYB has become a mature technique in terms of process protocol and welding capability.

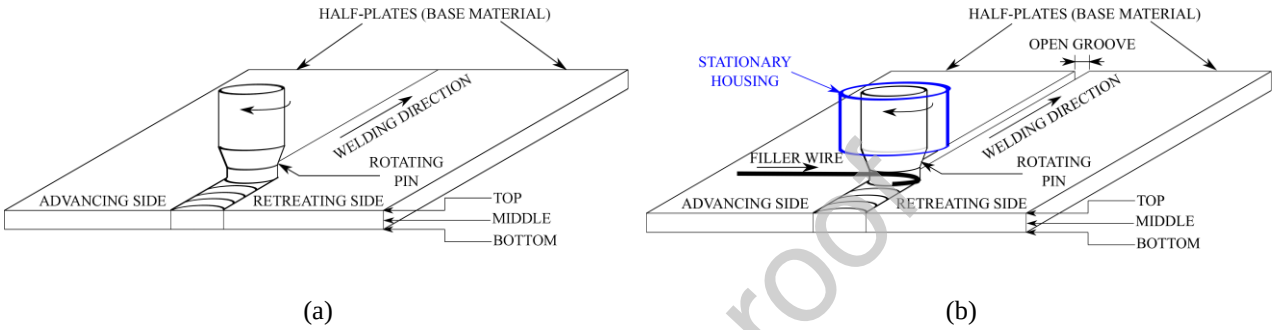

Figure 1: Schemes of the welding processes. (a) Friction stir welding. (b) Hybrid metal and extrusion bonding, which relies on a continuous extrusions and injection of a filler wire into the open groove to consolidate the weld.

The beneficial effects of the FM on the bending strength, tensile strength and fatigue life of a 2 mm thick similar AA6060-T6 HYB butt weld filled with AA6082-T4 were experimentally investigated in [12]–[14]. In [12], [13] a minor kissing bond defect between base and filler materials was unveiled, which promoted the crack initiation, especially during the three-point bending test. Nevertheless, the bending response of the joint approached that of the BM [12]. Furthermore, the yield stress (YS) evaluated through tensile tests was close to that reported for an equivalent FSW AA6082-T6 butt weld and superior to that of a FSW AA6061-T6 butt weld. Finally, the high-cycle fatigue property of this joint was characterised. After the removal of the kissing bond area, the joint exhibited the highest number of cycles to failure under constant amplitude loading, with respect to the comparable FSW and fusion welded joints considered in the literature [14].

Solid-state welding also aims at mitigating the thermal gradient effects involved, nevertheless it is impossible to completely eliminate them. Consequently, residual stresses arises in

correspondence of the weld heterogeneously distributed [2], giving rise to different residual stress types according to their length-scales [15], [16]. Given the nature of residual stress, i.e. a self-equilibrated stress in absence of external forces applied, it is not straightforward to detect its presence. Mainly for this reason, residual stress is often totally overlooked during the design against failure process of engineering components. The effect of residual stress can be either detrimental or beneficial to the structural integrity of designed components, depending upon its sign (i.e. compressive or tensile) at the most critical regions [17]. In the particular case of fatigue loading, the presence of residual stress modifies the actual mean stress and, in turn, it affects the durability performance of the material or component [18]–[20]. It is therefore evident that tensile residual stress is detrimental if present at locations where the effect of externally applied forces already generates a tensile stress field [21], [22]. Therefore, the material load-bearing capacity would be reduced, and the component may experience a premature failure. On the other hand, compressive residual stress is thought to be beneficial in most of the cases [17]. For this reason, in the past years several surface treatments, such as shot peening, have been developed to deliberately introduce compressive residual stress at the free surface of components [23].

The influence of residual stress on structural integrity has motivated the need of assessing residual stress also in welded structures [24]–[26]. Particularly for FSW, several studies have been performed exploiting different experimental methods: X-ray diffraction (XRD) [27], synchrotron XRD [28]–[30], neutron XRD [31], [32], FIB-DIC [29], and nanoindentation [32]. These techniques aim to investigate residual stress concerning the longitudinal, transverse and normal direction of the weld. Unfortunately, they are expensive, demanding and conditioned by the microstructure and weld material inhomogeneities. Despite this, XRD and neutron XRD have been recently used to investigate residual stress in an isothermal-FSW stainless steel plate [33]. Given that the dominant component of residual stress is that aligned with the weld direction, i.e. the

longitudinal one, as investigated in [27], [28], [31], [33], it is of interest to study only this component.

A practical solution to this problem, is the Contour Method (CM), a destructive technique developed at the Los Alamos National Laboratory about twenty years ago [34]. The method involves cutting a residual stress affected workpiece in half following a straight line. As a consequence, the obtained cut surfaces experience out-of-plane deformation due to the elastic relaxation of residual stress. Upon experimentally measuring this deformation (displacement) of the material, the obtained information can be prescribed in a Finite Element (FE) model. In particular, this model consists of an undeformed three-dimensional plate. Subsequently, the displacement field obtained from the previous experimental measurement is changed in sign. Finally, this field is imposed as the normal displacement boundary condition over the thickness of the plate model where the cut was supposed to occur. Such an operation allows the user to back-calculate the initial residual stress that was present prior the actual cut had occurred [34]. The major limitation of the CM is that the normal component of the displacement allows for evaluating only the component of the residual stress normal to the cut surface. Nevertheless, it is suitable for evaluating the dominant residual stress component due to the welding operation. If the cut is performed perpendicularly to the weld direction, the dominant residual stress component will be that normal to the cut surface, i.e. parallel to the weld direction. One of the significant advantages of the experimental methods based on the stress relaxation phenomenon, over the other non-destructive techniques, is that it provides an absolute evaluation of residual stress. Moreover, CM evaluates full-field residual stress at the macro scale, therefore it is not capable of capturing micro-scale effects due to material microstructure and inhomogeneities.

Over the past years, the CM has been extensively employed to study residual stress in thin, thick, similar and dissimilar FSW joints. For instance, as concerned aluminium joints, the CM was applied to investigate residual stress in a 25.4 mm thick dissimilar FSW plate made of AA7050-

T7451 and AA2024-T351 [35] and for the residual stress assessment of a 4 mm and a 8 mm similar AA6061-T6 FSW butt welds [36]. This experimental technique was also exploited to analyse the influence of welding process parameters on the arising of residual stress [37], where a set of 4 mm thick similar AA2024-T3 butt welds were considered. Dissimilar joints were also studied using the CM. For instance, the residual stress assessment was performed on a 2 mm thick plate made of aluminium 5A06 and T2M pure copper [38]. Recently, the residual stress has been evaluated in a 5 mm thick plate made of AA7075-T6 and AA6061-T6 strengthened with SiO_2 nanoparticles [39]. With regard to the FSW manufacturing technology, the CM was employed to investigate the residual stress induced by the innovative ultrasonic-assisted FSW. In this respect 3 and 5 mm thick similar AA6061-T6 were considered as a case-study [40], [41].

Besides affecting the structural performance, residual stress induced by manufacturing processes is responsible for joint distortion as well [42], [43]. In the context of FSW, for instance, the joint distortion of a FSW butt weld on a 3 mm thick plate made of AA6065-T6 was analysed in [44]. This study showed that residual stress, which peaked at about 200 MPa at the advancing side, generated the peculiar "V-shaped" angular distortion along the traverse direction. A recent research attempted to determine the dependence of the joint distortions upon the FSW welding parameters, i.e. pin rotation speed and welding feed speed [45]. In this work, a set of three FSW butt welds were manufactured on 3 mm thick AA6005-T6 plates, and essentially an "A-like" shape joint distortion was detected. However, earlier findings revealed that for a particular selection of pin rotation speed and welding feed speed, respectively 1200 rpm and 282 mm/min, the joint distortion turned out to be essentially negligible [46]. This was observed on a 6.5 mm thick FSW butt welded AA6061-T6 plate.

The present work aims to study and compare the residual stress arising as a consequence of the two solid-state welding processes just outlined, i.e. FSW and HYB. To date, no information regarding the residual stress state of HYB is available. This aspect is of fundamental importance in

order to establish its structural integrity performance and to assess how it performs as compared with the more conventional solid-state weld, i.e. FSW. The full-field residual stress evaluation of the welds is conducted by employing the CM. Statistical evaluation of errors, due to the mismatch of the residual stress evaluated on two different faces obtained by the linear cut, is performed and presented. Alongside, a quantitative analysis of the distortion of the FSW and HYB joints is reported. The results of the experimental analysis and comparison between the two case-studies are presented and critically discussed, with particular emphasis on the consequence that residual stress may have on the integrity properties of the examined welds.

3 Materials and Methods

This section of the paper reports a detailed description of the materials involved in the present study, along with the numerical and experimental methods employed. As concerns the materials, an extensive description of geometries, dimensions and process parameters of the two studied welds is presented. Regarding the methodologies involved in this study, an extensive overview of the CM is presented at first, then the details of the application of this method in the present work are thoroughly explained.

3.1 Welds preparation

Both the HYB and the FSW butt welds were prepared using extruded profiles of the commercial aluminium alloy AA6082-T6 as the BM. For the particular case of HYB, a AA6082-T4 was employed as the FM. Same materials were previously used by some of the authors of the present research and reported in the literature [47]. The nominal compositions of the base and filler materials are summarised in Table 1. The geometry of the plates is depicted in Fig. 2, while their dimensions are reported in Table 2.

The employed process parameters used to fabricate the HYB weld are given in Table 3. Because of confidentiality issues, the authors could not share the FSW parameters. Nonetheless, the applied welding parameters for HYB and FSW were deemed to represent best-practice at the time when the butt welds were manufactured. In particular, the welding parameters were tuned to produce the butt welds meeting all the acceptance criteria for offshore use [47].

The mechanical integrity of two identical HYB and FSW joints were previously investigated through their longitudinal tensile testing [47], and the related results are summarised Table 4. Besides, the data regarding the yield stress and ultimate tensile stress can be found in [48]–[51]. Before being extruded to perform the HYB weld, the wire FM underwent drawing that reduced its diameter from 1.6 mm to 1.4 mm. As a consequence, the FM experienced work hardening. For this

reason, at room temperature, the FM is characterised by the highest yield stress as compared with the BM.

With regard to HYB, it should be noted that if the FM was in the T6 condition, the high temperatures developed within the process zone of the weld would have triggered an overaging effect, which is well known to reduce the tensile strength of the material. Conversely, having the FM in T4 condition implied that most of the major alloying elements, such as Mg and Si, were in solid solution prior to the welding operation. Therefore, the natural ageing was preserved after the whole process. This ensured superior tensile properties as compared with those that would have been obtained if the FM was of the same type of the base material (BM). It this respect, the yield stress of the consolidated FM turned out to be about 70% of that of the BM [47], [52].

	Si	Mg	Cu	Fe	Mn	Cr	Ti	Zr	B	Other	Al
AA6082-T6 (BM)	1.00	0.65	0.03	0.20	0.50	-	0.02	-	-	-	Balance
AA6082-T4 (FM)	1.11	0.61	0.002	0.20	0.51	0.14	0.043	0.13	0.006	0.029	Balance

Table 1: Chemical compositions of the base and filler materials (wt%).

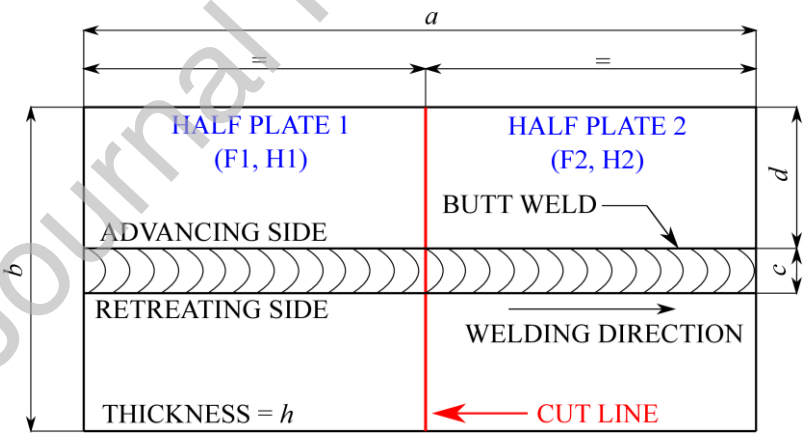

Figure 2: Scheme of the plates geometry. Each plate is characterised by a length *a*, a width *b* and a thickness *h*. The butt weld position is indicated by *d*, whereas its width is denoted by *c*. According to the CM procedure, the cut line in red, indicates the path followed to cut the plates in half. The cut provided the half-plates F1 and F2, and H1 and H2, for the case of FSW and HYB, respectively.

	a	b	c	d	h
HYB	500	170	14	79	4.2
FSW	770	168	18	70	4

Table 2: Plates dimensions (mm) in agreement with Figure 2.

	Groove width [mm]	Pin Rotation Speed [rpm]	Welding Feed Speed [mm/min]	Wire Feed Rate [mm/min]	Gross heat input [kJ/mm]
HYB	2	350	1080	7500	0.11

Table 3: Welding parameters for HYB. Those for FSW are not available due to confidentiality issues.

	Yield stress	Ultimate tensile stress
HYB	163	254
FSW	175	281

Table 4: Mechanical properties of the joints with respect to the longitudinal direction of the weld (MPa).

3.2 Contour Method

Although the entire CM protocol can be considered as well-established, considerable attention should be paid when selecting both the necessary experimental and numerical tools.

Wire electrical discharge machines (WEDM) have been recognised as the favoured equipment to perform the cut, provided that a rigid clamping of the specimen being cut is guaranteed. WEDM minimises plasticisation effects, which is a mandatory requirement to avoid interference with the residual stress already present in the specimen. Furthermore, the WEDM process should be tuned according to several parameters, such as the diameter, material and tension of the wire, and cutting speed. If these process parameters are not correctly tuned, local irregularities will occur, for instance, due to wire breakage. Moreover, wire vibrations can lead to surface-wide defects such as convex, concave or wavy cut surfaces. Lastly, low cutting speeds are preferred to provide low-roughness cut surfaces [53]. Recent studies showed how residual stress can arise as a consequence of the WEDM process, fortunately, this effect seems to be negligible when dealing with aluminium alloys [54].

Coordinate measuring machines (CMM) with a contact probing system, can be used to measure the elastic relaxation after the cut, given their high accuracy and wide availability. The raster-scan pattern that CMMs follow, basically a grid, requires a sufficiently fine nodal spacing to capture all the meaningful details of the relaxation over the cut surface.

In order to transfer the experimental findings into a FE analysis, this set of data requires a fitting process, usually with bivariate splines, to obtain an interpolated function. Consequently, the following critical quantities must be carefully selected: the grid node-spacing, the spline parameters (degree and nodes), and the FE element mesh size. The selection of such parameters strongly depends upon the specimen being analysed, nevertheless their choice can be addressed following the set of empirical rules proposed in the literature [53], [55].

Although the CMM workflow is consolidated, researchers or engineers using this method usually have developed their own simulation codes. Nevertheless, lately some open-source codes have been made available, such as pyCM [56].

3.3 Contour Method Application in the Present Study

The analysed plates were cut in half by means of the CDM Rovella 650© WEDM following the red line in Fig. 2 at a cut speed of 5 mm/min. The WEDM was equipped with a 0.25 mm diameter brass coated wire whose core composition was CuZn36. The cut of the two plates, respectively HYB and FSW, produced four half-plates. According to Fig. 2, H1 and H2 indicate the HYB half-plates, whereas F1 and F2 indicate the FSW half-plates. The index P is then defined, which can assume H1, H2, F1 and F2 to refer to a generic half-plate. Accordingly, the cut generated surface of the half-plate P will be denoted by Ω_P.

Owing to the WEDM cut, the half-plate P experienced an elastic relaxation that promoted the out-of-plane deformation of Ω_P. The measurement of this deformation was carried out using the Hexagon Global S© CMM with a contact probing system. The CMM had a resolution estimated to

be 1μm, whereas the probe was a 1 mm diameter ruby spherical tip. Fig. 3 shows the CMM measurement process of the half-plate Ω_{H1}.

In agreement with the arbitrary reference frame $\{O, x, y, z\}$ defined in Fig. 4(a), the generic point of Ω_P will be denoted by (x, y). Conforming to this reference frame, the elastic relaxation of Ω_P is oriented with respect to the z-direction, and it will be denoted by u_z^p.

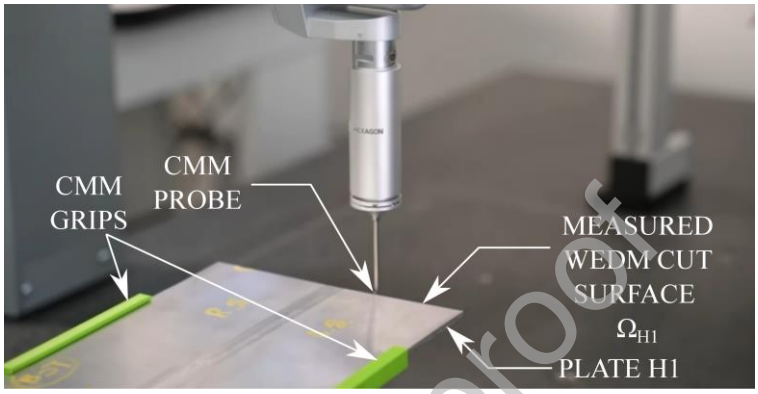

Figure 3: Example of CMM measurement carried out in this work. The half-plate H1 was firmly clamped by a set of customised grips. The CMM probe measured the out-of-plane displacements on the cut surface Ω_{H1}.

In order to measure u_z^p the CMM followed a raster-scan pattern defined over Ω_P. Such a pattern covered a rectangular grid with a regular 0.75x0.25 mm grid-spacing regarding the x and y-direction, respectively. According to Fig. 4(b), the grid nodes are identified by the couple of coordinates (x_g, y_g). The same grid-spacing was chosen for each pair of half-plates, given that their dimensions were similar. Thus, a set of four displacement maps was collected: $u_z^{H1}(x_g, y_g)$, $u_z^{H2}(x_g, y_g)$, $u_z^{F1}(x_g, y_g)$, $u_z^{F2}(x_g, y_g)$. In order to accurately match the axes of the Cartesian coordinate system for the experimental measurement and those of the numerical model, seen in Figs. 4(a)-(d), the Singular Value Decomposition was exploited. More details about the Singular Value Decomposition approach are provided in the Appendix of the present paper.

Bivariate splines were adopted to interpolate the acquired CMM data $u_z^P(x_g, y_g)$. These splines were of third- and second-order, and had 27 and 7 nodes both concerning the x- and y-

direction, respectively. These spline fitting parameters were judiciously chosen to obtain a good compromise between noise reduction and accuracy in capturing the relevant gradients and absolute values of displacements. The interpolation of $u_z^P(x_g, y_g)$ provided the functions denoted by $\mathfrak{u}_z^P(x, y)$ (Fig. 4(c)), thus: $\mathfrak{u}_z^{H1}(x, y)$, $\mathfrak{u}_z^{H2}(x, y)$, $\mathfrak{u}_z^{F1}(x, y)$, $\mathfrak{u}_z^{F2}(x, y)$.

In order to model the geometrical characteristics of the probed surfaces, the perimeter of the projection of $u_z^P(x_g, y_g)$ onto the x-y plane was computed, and this perimeter enclosed the surface Ω_P. Such a surface was then extruded to generate the three-dimensional solid body, with the actual length of the experimentally tested half-plates (Table 2). Subsequently, the generation of the mesh was performed following two steps using Gmsh [57]. Firstly, a mesh was generated over the enclosed surface, where 28 and 160 elements were prescribed concerning the thickness and width of Ω_P, respectively. The best-practice guidelines recommend to choose a FE size less than a quarter of the spline nodal spacing with respect to both x- and y-direction [53]. The selected number of elements along with the adopted spline nodal spacing complied with such an empirical rule. In addition, a selective mesh refinement was performed in the neighbourhood of the weld region, in order to better capture possible sharp variations of residual stress. Secondly, the mesh was extruded along the third direction by imposing a finer mesh near Ω_P and coarser far from Ω_P. These steps provided meshes counting 89600 volume elements. Fig. 4(d) shows an example of the mesh structure without complying with the actual number and dimensions of the elements. The generic mesh node of Ω_P will be indicated as (x_m, y_m).

The FE simulation was carried out using code_aster, a FE open-source code. As discussed earlier, the spline was interpolated at and among all the mesh nodes (x_m, y_m) of Ω_P. The obtained displacement map was then changed in sign, thus providing $-\mathfrak{u}_z^P(x, y)$ (Fig. 4(c)). Finally, this map was prescribed as a boundary condition over Ω_P. In addition, the rigid body motion was suppressed by adding further constraints but avoiding statically indeterminate conditions. In particular, it was sufficient to eliminate the rigid body motions about the x- and y-direction, respectively. This is

represented in Fig. 4(c) by the red nodal hinges. A linear elastic behaviour was considered for the FE analysis, given that it is hypothesised that the residual stress relaxation does not give rise to significant plastic deformations. Eight-node brick elements with linear shape functions were utilised in the FE analysis. These elements are called HEXA8 according to code_aster nomenclature. As was mentioned in the Introduction, the CM evaluates residual stress at the macro scale, therefore the studied aluminium alloys were assumed to be homogeneous and isotropic. Their Young's modulus and Poisson's ration were reasonably assumed to be E = 70000 MPa and ν = 0.3.

As a result of the FE simulation, the longitudinal component of the residual stress due to the welding process, namely $\sigma_{zz}^{P}(x,y)$, was back-calculated. Fig. 4(d) shows an illustrative example of a contour of $\sigma_{zz}^{P}(x,y)$, where red and blue schematically represent tension ($\sigma_{zz}^{P} > 0$) and compression, ($\sigma_{zz}^{P} < 0$) respectively. In total, the following set of residual stress maps was computed $\sigma_{zz}^{H1}(x,y)$, $\sigma_{zz}^{H2}(x,y)$, $\sigma_{zz}^{F1}(x,y)$, $\sigma_{zz}^{F2}(x,y)$.

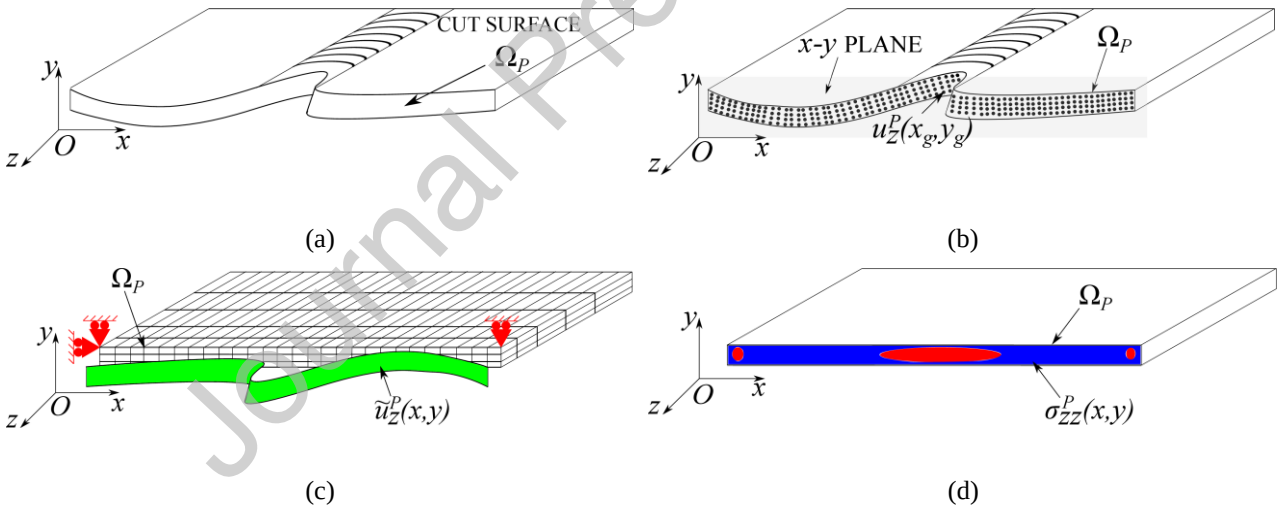

Figure 4: Contour Method steps for the analysis of the *P*-th half-plate. (a) After the WEDM cut, *P* exhibited an elastic relaxation which had forced the material inward the cut surface Ω_P. (b) The cut surface Ω_P was probed using a CMM obtaining the displacement map $u_z^P(x_g, y_g)$, where x_g and y_g are the points of the raster-scan pattern defined onto Ω_P. (c) The map $u_z^P(x_g, y_g)$ was spline-fitted and changed in sign, providing the function $\tilde{u}_z^P(x,y)$. A FE model of the half-plate *P* was designed and $\tilde{u}_z^P(x,y)$ was prescribed over the plate thickness where the WEDM cut was supposed to occur. In addition, the red nodal nodal hinges indicate the suppressed rigid body motions. (d) The FE simulation back-calculated the residual stress $\sigma_{zz}^P(x,y)$, over the cut surface Ω_P, that was present prior to the cut.

Given that prior the WEDM cut, the couples of cut surfaces Ω_{H1} and Ω_{H2}, and Ω_{F1} and Ω_{F2} shared exactly the same stress state, in correspondence of the discrete surface the back-evaluated residual stress values must be coincident with each other. As a consequence, it is appropriate to obtain a unique evaluation of residual stress for each plate. Thus, the residual stress estimator for a plate was defined as:

$$\sigma_{zz}^{HYB}(x,y) = \frac{\sigma_{zz}^{H1}(x,y) + \sigma_{zz}^{H2}(x,y)}{2} \quad (1)$$

$$\sigma_{zz}^{FSW}(x,y) = \frac{\sigma_{zz}^{F1}(x,y) + \sigma_{zz}^{F2}(x,y)}{2} \quad (2)$$

Besides, the standard deviation of the estimators for a generic plate was also computed:

$$U_{zz}^{HYB}(x,y) = std\left(\sigma_{zz}^{H1}(x,y), \sigma_{zz}^{H2}(x,y)\right) \quad (3)$$

$$U_{zz}^{FSW}(x,y) = std\left(\sigma_{zz}^{F1}(x,y), \sigma_{zz}^{F2}(x,y)\right) \quad (4)$$

Much attention was devoted to three critical paths over the surface Ω_P: the top (*T*), the middle thickness (*M*) and the bottom (*B*), see Fig. 1. According to Eqs. (5)-(6), an index *K* is defined, which can assume *T*, *M* and *B*, to refer to a generic path. Then the residual stress $\sigma_{zz}^{P}(x,y)$ was extracted along a line positioned at each path *K*. In the following, $\sigma_{zz}^{P}(K)$ and $U_{zz}^{P}(K)$, will denote the residual stress σ_{zz}^{P} and U_{zz}^{P} extracted along the path *K*. Therefore for each path *K*, the related residual stress estimator was:

$$\sigma_{zz}^{HYB}(K) \pm U_{zz}^{HYB}(K) \quad (5)$$

$$\sigma_{zz}^{FSW}(K) \pm U_{zz}^{FSW}(K) \quad (6)$$

The common CM protocol implies to align and average the displacement maps of the two WEDM cut surfaces, thus resulting in a single displacement map. The averaged map is then spline-fitted, applied as a boundary condition onto the FE model and eventually the FE simulation is

conducted [34], [53]. Although a single FE simulation is required, the common protocol does not provide a measure of uncertainty on the final result.

The followed procedure slightly differed from such a protocol, given that the cut surfaces were independently analysed, thus maintaining the displacement maps as separated. As a consequence, two related FE were required. Although this was a slight, yet elaborated, variation to the common CM procedure, it directly provided a practical measure of uncertainty related to the repeatability (Eq. (3)-(4)), along with the evaluation of the residual stress (Eq. (1)-(2)).

4 Results and Discussion

This section aims at presenting the results of the analysis of two crucial aspects arisen from the considered solid-state welding processes: the weld transverse distortion and the residual stress. The transverse distortion results of each cut surface *P* are shown and discussed. Regarding the results of the CM evaluation of the HYB- and FSW-induced residual stress, these are then given and critically discussed. Additionally, all these results are cross-compared to highlight similarities and differences between the two solid-state welding processes.

4.1 Weld Distortions

According to the literature, research has been devoted to study the relationship between FSW-induced residual stress and the correspondent weld distortion. Identifying such a relationship, however, was out of the scope of the present paper. Nevertheless, it is useful to report a qualitative analysis of the distortions of the welds and discuss how they compared with the results from the literature.

The boundary of the x-y plane projection of $u_z^P(x_g, y_g)$ was numerically post-processed to calculate the joint distortion of the considered samples, in correspondence of the cut surfaces Ω_P. Fig. 5(a) shows the boundaries of Ω_{H1} and Ω_{F1} , whereas Fig. 5(b) shows those of Ω_{H2} and Ω_{F2}. The HYB distortion was characterised by the deflection angle γ, evaluated with respect to the middle-thickness line (Figs. 5(a)-5(b)). The angle γ turned out to be equal to 181.62° for H1 and 181.07° for H2. The HYB half-plates exhibited a "V-shaped" distortion, which could be quantified by the peak-to-valley range of the middle-thickness lines. These ranges are about 1 mm and 0.8 mm for H1 and H2, respectively. Although Ω_{H1} and Ω_{H2} were the counterpart of each other, thus the peak-to-valley ranges should be equal, the authors believe that this discrepancy could be justified by an uneven residual stress relaxation effect. Moreover, the approximatively 0.5° of distortion present between the two cut plates is negligible and can be due to several factors which are not strictly related to the residual stress evaluation conducted in this study, i.e. inhomogeneous plastic

deformation in the transverse direction along the welding direction, CMM errors which become amplified through the calculation process. As far as F1 and F2 are considered, their joint distortion are so modest that it was not possible to detect them according to the CMM resolution (Figs. 5(a)-5(b)). Therefore, at this qualitative level of analysis the deflection angle γ and the peak-to-valley range, can be assumed as 180° and 0 mm for both F1 and F2. This negligible distortion was also observed in the 306x306x6.5 mm AA6061-T6 FSW butt weld analysed in [46]. Despite that the plate geometry analysed in this work is slightly different to that of [46], the results are in good agreement with each other. Interestingly, a characteristic "V-shaped" distortion was also encountered with regard to a 600x315x3 mm AA6065-T6 FSW butt weld found in the literature [44].

The higher HYB joint distortion may reasonably prompt to think that the HYB plate accommodated higher residual stress than the FSW plate. Nevertheless, the authors of [45] identified an inverse relationship between joint distortion and residual stress for a FSW 220x110x3 mm AA6005-T6 plate. From a practical viewpoint, they showed the more distortion the less residual stress. Thus, no qualitative results about residual stress can be fairly inferred with regard to the HYB butt weld.

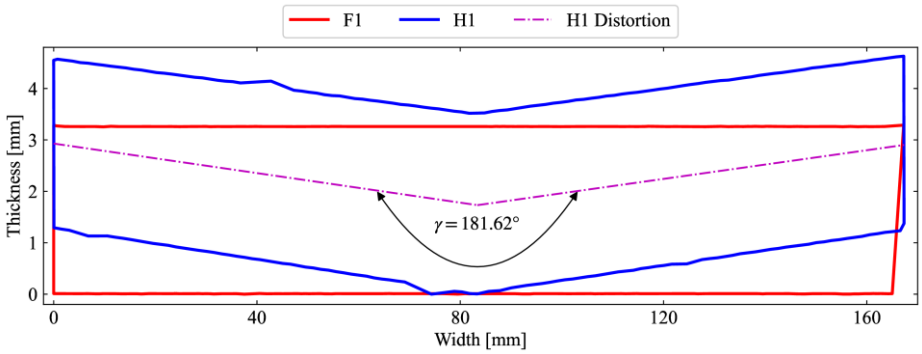

(a)

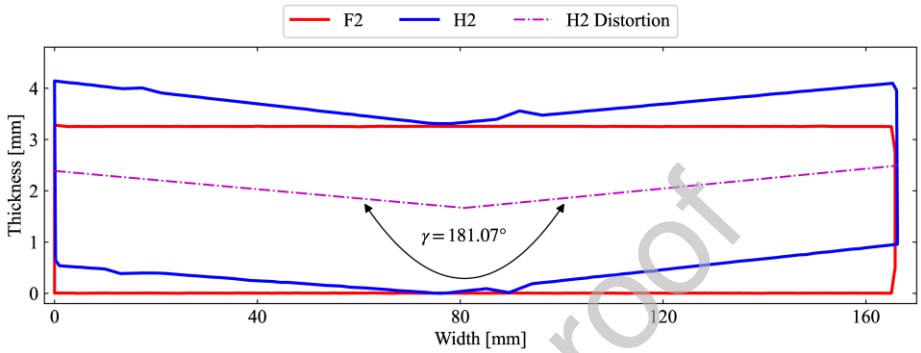

(b)

Figure 5: Boundaries of the cut surfaces Ω_P and characterisation of the transverse distortion for the HYB half-plates. The blue and the red lines represents the boundaries of the HYB and FSW half-plates, respectively. The purple dot-dashed line is the middle-thickness line of the HYB half-plates where the deflection angle γ was evaluated. (a) Boundaries of Ω_{F1}(red) and Ω_{H1} (blue). (b) Boundaries of Ω_{F2} (red) and Ω_{H2} (blue). The cut surfaces Ω_{H1} and Ω_{H2} exhibited a more pronounced traverse distortion as compared with their FSW counterpart Ω_{F1} and Ω_{F2}.

4.2 Residual stress

Figs. 6(a)-6(d) show the displacement maps of the elastic relaxation $u_z^P(x_g, y_g)$, for H1, H2, F1 and F2. Since the z-position of the reference measurement plane x-y is arbitrary, the data were translated to the mean value of the correspondent $u_z^P(x_g, y_g)$ [53]. Quantitatively, the relaxation ranged from -0.07 mm to 0.06 mm for H1 and H2, and from -0.05 mm, 0.04 mm for F1 and F2. In addition, the measured relaxations $u_z^{F1}(x_g, y_g)$ and $u_z^{F2}(x_g, y_g)$ are consistent both in order of magnitude and in shape with those observed for the 300x206x4 mm AA6061-T6 FSW butt welds in [36]. In the present study, the weld region is enclosed between x=79 mm and x=93 mm for H1 and H2 half-plates, while for F1 and F2 this region lies between x=70 mm and x=88 mm. Inside these regions it is possible to recognise $u_z^P(x_g, y_g) < 0$. These physically means that the material over

each cut surface Ω_P relaxed due to the presence of tensile residual stress and therefore the cut surface was subjected to out-of-plane displacement pointed in the inward surface direction. Despite the shape of the relaxation of H1 and H2 is similar to that of F1 and F2, HYB half-plates show higher magnitudes of relaxation. Consequently, higher tensile residual stress was already expected to be present in H1 and H2. These qualitative observations are further corroborated by the CM evaluations.

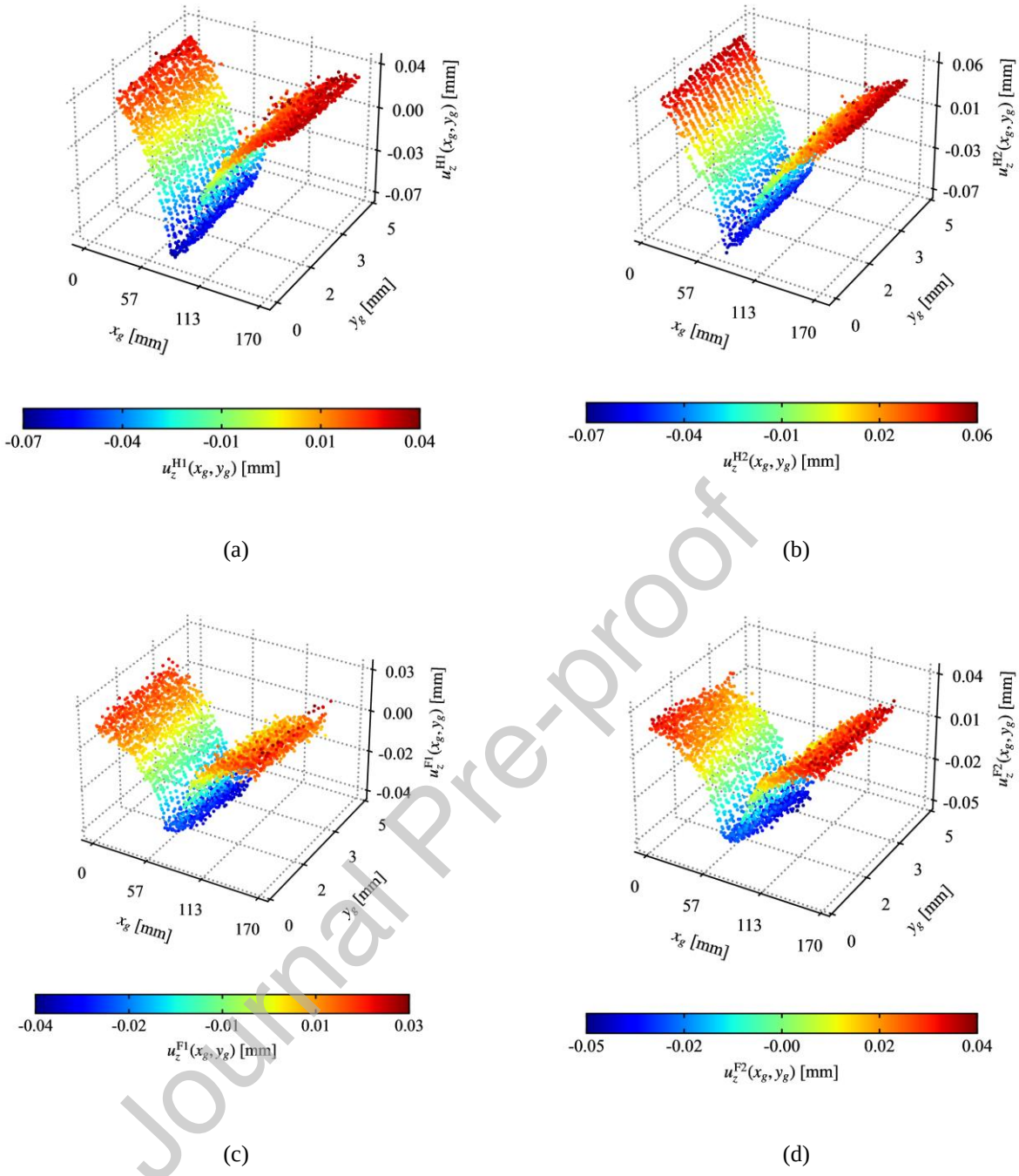

Figure 6: CMM-measured displacement maps $u_z^P(x_g, y_g)$ of the elastic relaxation of *P*-th cut surface. All the half-plates were subjected to a relaxation which forced the material inward the correspondent cut surface. (a) *P*=H1 (b) *P*=H2 (c) *P*=F1 (d) *P*=F2.

The application of the CM provided the contours (Figs. 7(a) - 7(d)) of the residual stress induced by the two solid-state welding methods employed, namely $\sigma_{zz}^P(x, y)$, for H1, H2, F1 and F2. All these contours clearly identify a predominant tensile residual stress inside the weld and

milder compressive residual stress in the regions outside the weld. The residual stress distributions of F1 and F2 agree both in terms of trend and order of magnitude with other comparable CM evaluations for 4 mm thick aluminium FSW butt welds, already present in the literature [36], [37]. In particular, regarding the order of magnitude, residual stress over the cut surfaces varying from - 150 MPa to 100 MPa were reported in [37], and from - 50 MPa to 100 MPa were reported in [36]. Furthermore, the contour maps highlight higher residual stress in H1 and H2, thus confirming the initial observation with regard to the relaxation ranges. Although the contours give a global picture of the residual stress over the cut surface, they do not capture the residual stress distribution with respect to the plate width. For this reason, the aforementioned three paths, *T*, *M* and *B*, were drawn onto the cut surfaces Ω_P, Figs. 7(a) - 7(d). These paths were conceived to follow the distortion of the half-plates. Therefore, those regarding H1 and H2 show the distinctive "V-like" shape, while those for F1 and F2 are horizontal. The residual stress extracted along these paths, $\sigma_{zz}^{P}(K)$, are depicted in the upper part of Figs. 7(a) - 7(d), as well as the weld position and the indication of the advancing side (AS) and retreating side (RS). The *T* and *B* paths, were taken slightly offset from the upper and the lower edges of the half-plate, given that inaccuracies might arise as a consequence of unstable spline interpolation at those boundaries. Moreover, the higher the spline order, the higher the instability is [58]. On the top of that, the residual stress evaluation might be less reliable near the perimeter of the cut surfaces for two main reasons: i) WEDM cutting artefacts; ii) a minor elastic deformation about the y-direction due to the elastic relaxation of the traverse component of residual stress.

The outcomes just outlined, however, only represent an intermediate result of the CM evaluation. In fact, these findings need to be combined using Eqs. (1)-(2) along with the evaluation of the associated uncertainties given by Eqs. (3)-(4) to obtain a more accurate evaluation of the residual stress fields for the two welds.

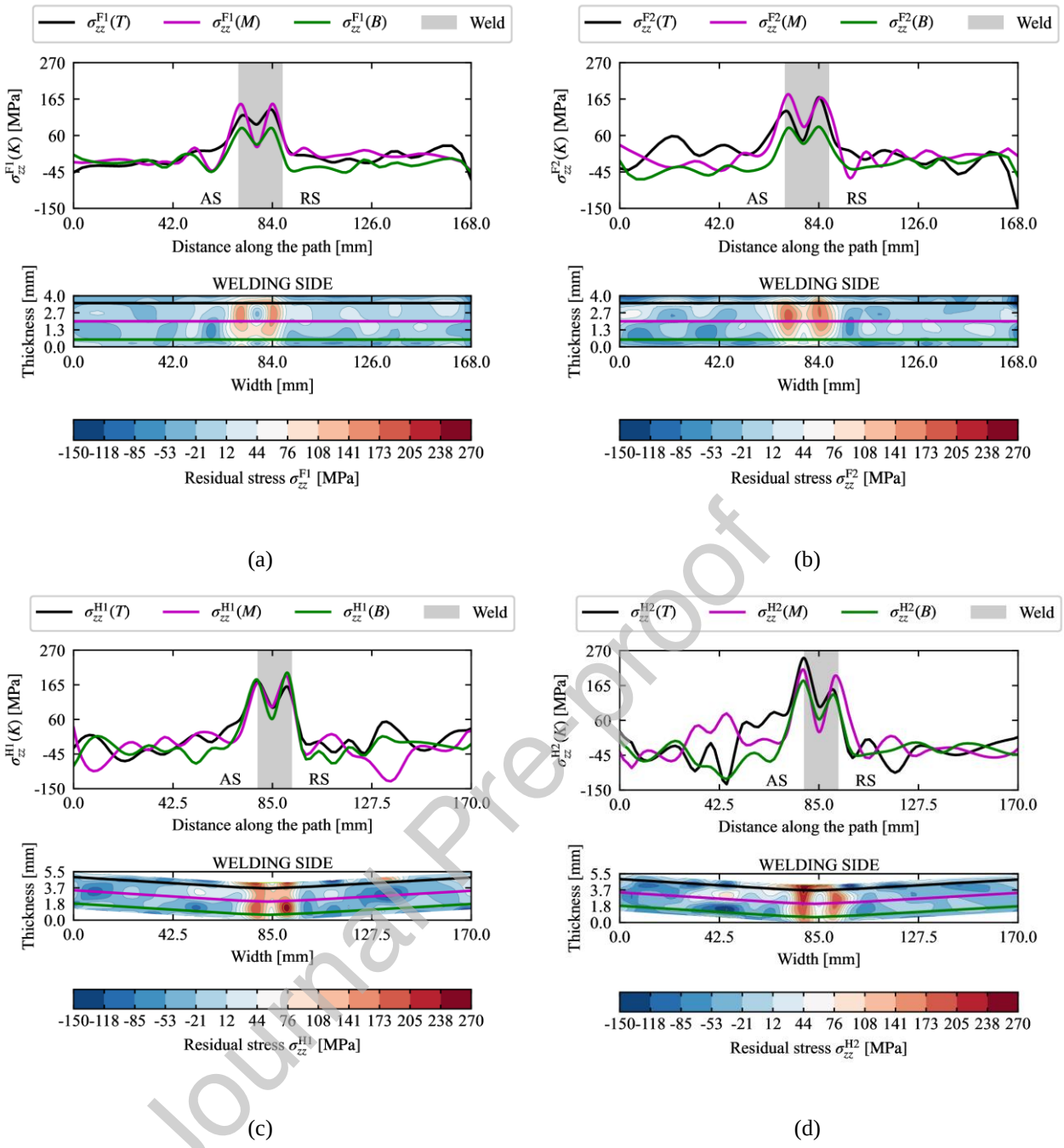

Figure 7: Results of the CM residual stress evaluation of each of the P-th cut surface. Each picture shows in its lower part the contour of the residual stress over the related cut surface Ω_P, namely $\sigma_{zz}^{P}(x,y)$. Three paths were drawn onto Ω_P to extract the residual stress data. With respect to the thickness of Ω_P, these path are located at its top (T), middle-thickness (M) and bottom (B). The residual stress extracted along the three paths are named $\sigma_{zz}^{P}(K)$ for K = T, M, B, and are shown in the upper part of each picture. Black, purple and green were respectively associated to the T, M and B paths in order to distinguish the extracted residual stress data. In addition, the advancing side (AS), the retreating side (RS) and the weld position are indicated. (a) P=F1. (b) P=F2. (c) P=H1. (d). P=H2.

The evaluated residual stress, extracted along the K path, $\sigma_{zz}^{P}(K)$, are depicted in Figs. 8(a)-8(d) and in Figs. 9(a)- 9(d), for the FSW and HYB half-plates, respectively. As far as the FSW butt

weld is concerned, the paths revealed the classical "M-shaped" pattern. This qualitative trend agrees well with earlier experimental studies on aluminium butt welds, 3 mm thick [28], 4 mm thick [37], 8 mm thick [27], and also with steel butt welds 3 mm thick [31], [33]. Intriguingly, a similar "M-shaped" pattern was retrieved for the HYB butt weld. Generally, all the paths show high tensile residual stress within the weld and a steep decrease moving towards the BM, reaching a compressive residual stress state, similarly to what reported by other researchers [37]. The observed oscillations right outside the weld could have been arisen for two main reasons: i) the heterogeneous intrinsic residual stress present in the BM due to its manufacturing process (extrusion), thus producing low-frequency oscillations; ii) the interpolation of the CM measurement noise which generates high-frequency oscillations. The latter class of fluctuations would have been reduced if the CMM measurements had been smoothed more. However, this in practice cannot be carried out since it would smear the significant gradients of residual stress, particularly those in correspondence of the weld affected zone; for instance the "M-like" shape inside the weld would have been aliased. For this reason, it appears to be very important to judiciously choose the most appropriate interpolation functions. According to Eqs. (5)-(6), the residual stress estimators and their associated interval bands are depicted in Figs. 8-9. These bands account for the CM evaluation repeatability and represent the values in the range $\sigma_{zz}^{FSW}(K) \pm U_{zz}^{FSW}(K)$ (Figs. 8(a)-(c)) and $\sigma_{zz}^{HYB}(K) \pm U_{zz}^{HYB}(K)$ (Fig. 9(a)-(c)). Therefore, the bands provide a confidence interval of approximately 68%. Given that narrower bands are present on the edge of the AS and RS, in such regions the evaluated $\sigma_{zz}^{FSW}(K)$ and $\sigma_{zz}^{HYB}(K)$ accurately predict the residual stress. However, wider bands were encountered in correspondence of the AS and RS peaks. Although a better estimation of the confidence intervals, may improve the accuracy of the estimated errors, for instance by performing more WEDM cuts on the same butt weld, the computed confidence intervals are appropriate to discuss the following result. To date, the user could refer to [59], in which the uncertainty quantification of the CM was addressed.

With regard to FSW, the combination of the peripheral speed of the pin and the welding feed speed is generally responsible for asymmetries between the two observed tensile residual stress peaks in correspondence of the heat-affected zone, in terms of magnitude. Physically, the relative speeds between the rotating pin and the BM is different between the AS and RS sides, respectively. This intrinsic feature of the FSW process, produces higher frictional heat at the AS and consequently more severe temperature gradients at the AS. Therefore, higher residual stress should be expected at the AS [35]–[38]. Concerning the *M* and *B* paths, Fig. 8(a) and Fig. 8(c), this behaviour is little intense, leading to comparable magnitudes of the two tensile peaks. However, the confidence interval of the *M* path does not preclude a more accentuated asymmetric behaviour. Conversely, the asymmetry is evident for the *T* path. Because of the analogy between HYB and FSW processes, the asymmetric tangential speed at the AS and RS lead to the same conclusion for the HYB, conceptually. Nonetheless, such an asymmetry is exacerbated (Figs. 9(a)-9(c)).

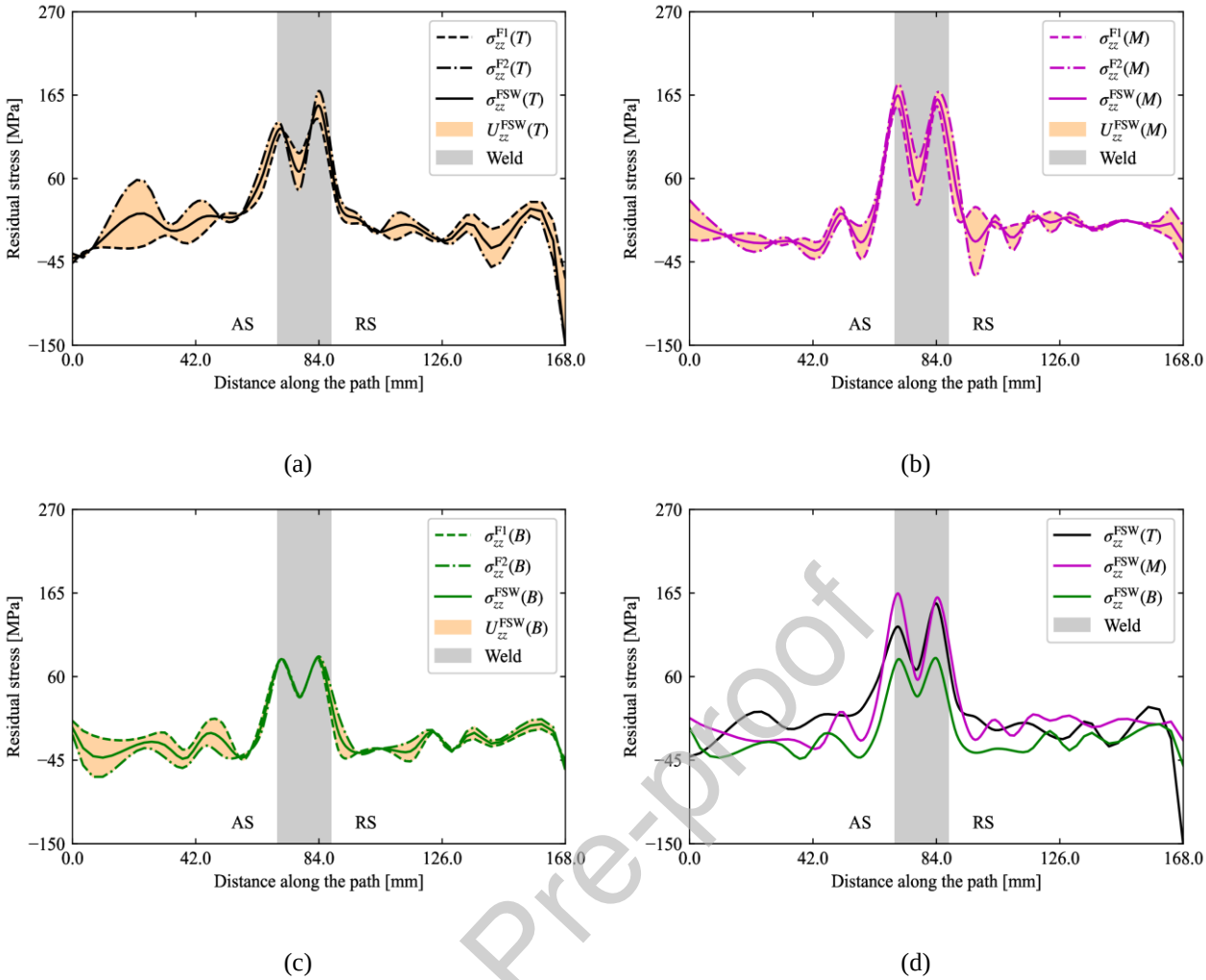

Figure 8: Residual stress estimator for the *K*-path$\sigma_{zz}^{FSW}(K)$ and associated uncertainty $U_{zz}^{FSW}(K)$ computed from $\sigma_{zz}^{F1}(K)$ and $\sigma_{zz}^{F2}(K)$ (Eqs. (2) and (4)). The filled area enclosed between $\sigma_{zz}^{F1}(K)$ and $\sigma_{zz}^{F2}(K)$ graphically represents $U_{zz}^{FSW}(K)$, thus corresponding to a confidence interval of about 68% for $\sigma_{zz}^{FSW}(K)$. (a) *K*=*T*. (b) *K*=*M*. (c) *K*=*B*. (d) Comparison between the residual stress estimators $\sigma_{zz}^{FSW}(K)$ evaluated along the path *K*=*T*, *M*, *B*. The advancing side (AS), the retreating side (RS) and the weld position are also indicated.

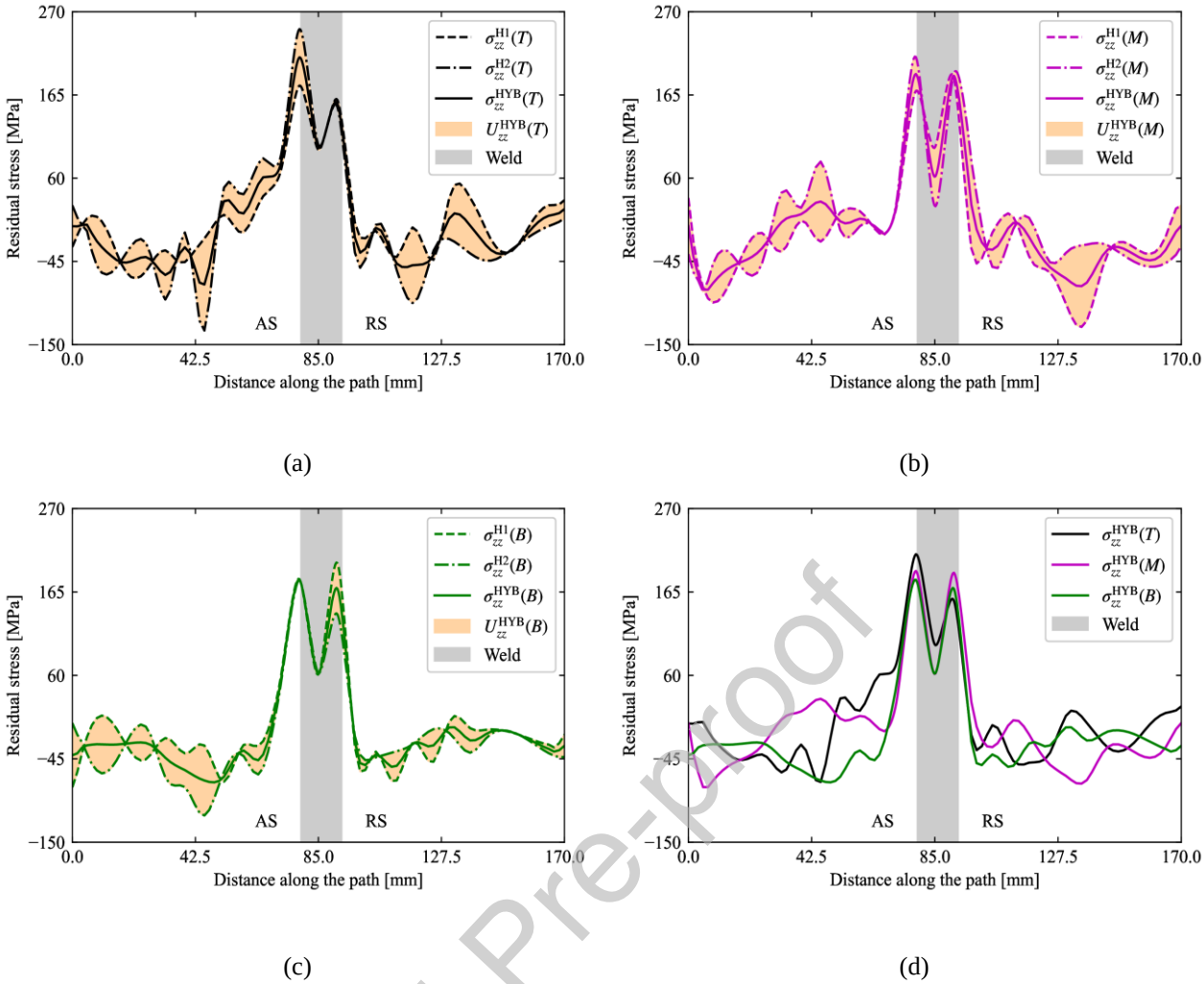

Figure 9: Residual stress estimator for the *K*-path$\sigma_{zz}^{HYB}(K)$ and associated uncertainty $U_{zz}^{HYB}(K)$ computed from $\sigma_{zz}^{H1}(K)$ and $\sigma_{zz}^{H2}(K)$ (Eqs. (1) and (3)). The filled area enclosed between $\sigma_{zz}^{H1}(K)$ and $\sigma_{zz}^{H2}(K)$ graphically represents $U_{zz}^{HYB}(K)$, thus corresponding to a confidence interval of about 68% for $\sigma_{zz}^{HYB}(K)$. (a) *K*=*T*. (b) *K*=*M*. (c) *K*=*B*. (d) Comparison between the residual stress estimators $\sigma_{zz}^{HYB}(K)$ evaluated along the path *K*=*T*, *M*, *B*. The advancing side (AS), the retreating side (RS) and the weld position are also indicated.

A critical comparison between the two analysed welds can underline several similitudes and differences. In the FSW weld the *M* path is the most critical, followed by *T* and *B*, in terms of highest magnitudes of residual stress, see Fig. 8(d). On the other hand, in the HYB joint the residual stress intensity within the weld is comparable, see Fig. 9(d). Quantitatively, the predicted residual stress peaked along the path *M* at the AS and at the RS at about 165±15 MPa and 155±5 MPa as concerns the FSW butt weld, whereas at 205±25 MPa and 180±5 MPa for the HYB butt weld. In order to provide an immediate comparison between these findings and those from the literature,

Table 5 was reported to summarise the welding process, the material, the welding parameters and the magnitudes of the residual stress peaks detected along the middle-thickness path (*M*). The present findings regarding the FSW sample concur well with those reported in the literature concerning the butt welds performed on AA6061-T6 plates 270x250x8 mm and 300x206x4 mm plates, even though different aluminium alloys were involved [36]. In [36], although the classical "M-like" shape pattern was not clearly distinguishable, analogous paths were analysed. In the totality of residual stress profiles reported in the literature, the middle-thickness path (*M*) turned out to be the most critical, followed by *T* and *B*, for both the analysed 4 mm and 8 mm thick FSW butt welds, which agrees with the results presented herein. Notwithstanding the different thickness, the residual stress magnitudes reached at the AS and RS were respectively 163 MPa and 100 MPa for the 8 mm thick plate, with a very good agreement with those found in the present study of the FSW. Similar agreement was also found with regard to the 4 mm thick plate from the literature, the residual stress peaked at the AS and RS at 154 MPa and 130 MPa, respectively. Additional support to this conclusion is provided by the results reported in [37], in which a full-factorial sensitivity analysis of FSW was addressed. The aim of the study was to establish the influence of the welding parameters on the induced residual stress. In particular, a set of AA2024-T3 200x30x4 mm FSW butt welds was analysed. Peak values of 145 MPa and 125 MPa were observed at the AS and RS, respectively. Such values were retrieved by combining a fixed welding feed speed of 140 mm/min with different pin rotation speeds from 800 rpm to 1600 rpm. Despite the different material employed in [37], the reported peak values are remarkably close to those found in the present study.

Welding process	Material	Butt weld dimensions [mm]	Pin rotation speed [rpm]	Welding feed speed [mm/min]	Wire Feed Rate [mm/min]	AS peak [MPa]	RS peak [MPa]	Source
FSW	AA6061-T6	300x206x4	800	300	-	154	130	[36]
FSW	AA6061-T6	270x250x8	500	250	-	163	100	[36]
FSW (full-factorial experiment)	AA2024-T3	200x30x4	800÷1600	140	-	145	125	[37]
FSW (this study)	AA6082-T6	770x168x4	-	-	-	165±15	155±5	Fig. 8(b)
HYB (this study)	AA6082-T6 (Base) – AA6082-T4 (Filler)	500x168x4	350	1080	7500	205±25	180±5	Fig. 9(b)

Table 5: Summary of the comparable CM evaluations of residual stress

Finally, from the cross-comparison between the HYB- and the FSW-induced residual stress along the *T*, *M* and *B* paths, it is evident that HYB produced higher residual stress magnitudes into the region affected by the joining process.

Apart from the continuous extrusion and injection of the filler material, HYB and FSW are two similar friction-driven welding methods. With regard to FSW, earlier studies has demonstrated the dependence of residual stress upon welding parameters and materials being welded [35]–[39]. Although the present research was the first attempt to characterise residual stress in HYB, the authors believed that different materials (BM and FM) and HYB welding parameters might influence the residual stress distribution as well.

It is worth observing that if unprocessed plates were involved, i.e. neither extrusion nor solid-state welding, in principle the CM would have provided null residuals stress over the WEDM cut surface. Nonetheless, measurement noise would have affected the CM evaluation by generating fluctuations in the final result. On the other hand, if the plates were extruded but not solid-state welded, only the residual stress inherited from the extrusion process would have been retrieved. Still, measurement noise might have affected the residual stress evaluation.

Light onto the origin of longitudinal residual stress in welding, or more specifically in FSW, was already shed [60]. To interpret this phenomenon, it is useful to consider small element volume of the BM AA6082-T6 located at the edge of the weld nugget. As far as the FSW is concerned, the blue solid line in Fig. 10 describes a schematic example of the temperature-stress history experienced by this volume. Fig. 10 also reports for the BM examples of tensile, σ_y^+, and compressive, σ_y^-, yield stress curves as a function of the temperature (black solid line). Besides, T_{max}indicates the maximum temperature which is expected to occur within the weld nugget. In addition, T_{melt}, is the melting temperature of the BM. Essentially, the approaching heat source (rotating pin) ensures that the considered volume of material increases its temperature (line AB in Fig. 10) and expands. This thermal expansion is constrained by the surrounding material and therefore a compressive residual stress is generated within the material at the heat source (line AB). Due to the combination of high temperature and high compressive residual stress, the material reaches the compressive yield stress (point B) and deforms plastically (line BC). As the heat source overtakes the same volume of material (line BC), a cooling process begins (point C) which makes the material to shrink (line CD). This shrinkage is again constrained by the surrounding material and therefore tensile stress takes place in the weld (point D). Given that the contraction occurs in the linear elastic regime of the material, in this instance, the amount of tensile stress generated is higher than the compressive stress arose in the expansion stage. For this reason, tensile residual stress is originated at the end of the welding (point D). In the particular case of FSW, the heat source is not uniform within the welding due to the higher friction generated at the material/tool interface, and for this reason two tensile peaks are generally found (Figs. 8(a)-(d)).

Regarding the HYB technique, same considerations done for the FSW still hold. Yet, a significant difference is made by the presence of a second material (FM) showing different elastoplastic properties (black dashed yield stress curve in Fig. 10) when compared with the BM. It is important to remark that the FM had undergone a drawing process before being employed in the

welding process. Such a wire-pre-process introduces work hardening that increased its yield stress level. Nevertheless, the work hardening effect is cancelled as soon as the material enters the rotating pin, thanks to the dynamic recovery triggered by the temperatures reaching values as high as 400 °C [61]. Therefore, most of the ductility of the FM is regained and the yield stress becomes lower than that of the BM. Furthermore, T_{max} and T_{melt} are supposed to be equal for the FM. The latter temperature is generally true, while the former might differ for the two processes. In fact, under some circumstances HYB might generate slightly lower temperatures than those of FSW [62]. Therefore, this physical interpretation can be considered valid as long as the difference between the maximum temperature due to HYB, and FSW, is negligible - it is the case of the present study. The red dashed line in Fig. 10 represents a schematic temperature-stress cycle of a small volume of FM AA6082-T4, which is located at the edge of the weld nugget. In this study, the FM shows a substantially lower yield stress. This characteristic makes sure that during the material expansion stage (line A'B), the FM builds up compressive stresses that are lower than what the BM would do (line AB). As a consequence, during the cooling stage (line C'D'), the constrained material shrinkage allows the residual stress to reach higher values of tension (point D').

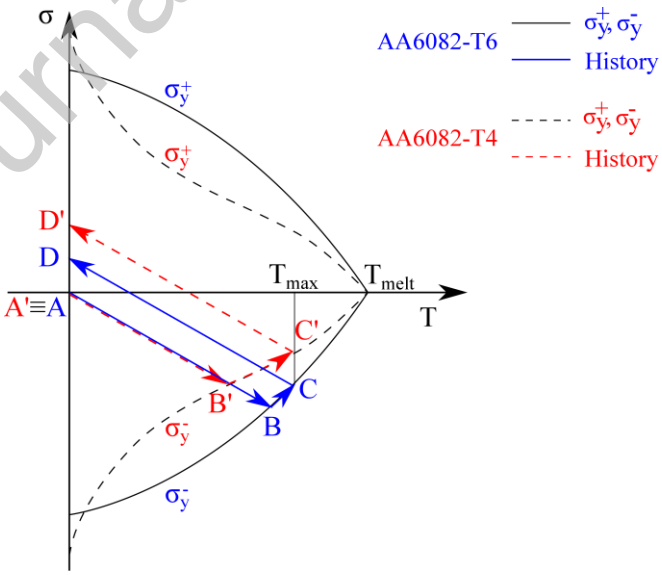

Figure 10: Temperature-stress cycles experienced by a small volume element of: BM AA6082-T6 (blue solid line ABCD) and FM AA6082-T4 (red dashed line A'B'C'D'). In both cases, such a volume element is assumed to be located at the edge of the weld nugget. The yield stress vs. temperature curve of the two materials are reported.

5 Conclusions

The present study considered a 4 mm thick AA6082-T6 HYB butt weld performed using an AA6082-T4 as the FM, and a 4 mm thick AA6082-T6 FSW butt weld. Specifically, the full-field longitudinal residual stress state of these joints was evaluated employing the CM. In particular, this research has addressed for the first time the residual stress evaluation in a HYB butt weld.

The residual stress analysis unveiled similar residual stress distributions for both HYB and FSW butt welds, i.e. tensile residual stress in the weld region and milder compressive residual stress within the neighbouring regions of the weld affected zone. The residual stress distributions exhibited two tensile peaks respectively observed at the AS and the RS of the FSW butt welds, describing the peculiar "M-like" shape residual stress pattern, also seen in other previous studies reported in the literature. Additionally, the "M-like" shape residual stress pattern was retrieved for the HYB butt weld. A key difference was revealed between the two welds, that is significantly higher tensile residual stress magnitudes present in the HYB, both at the AS and RS. Quantitatively, the residual stress attained its maximum at the AS at 205±25 MPa. By contrast, the FSW joint showed its maximum value of tensile residual stress at the AS as high as 165±15 MPa.

A physical interpretation has been proposed to explain the discrepancy in terms of residual stress magnitude between the analysed welds. In this respect, the higher residual stress in the HYB butt weld stemmed from the presence of the softer FM, which is exclusively employed in HYB. In fact, the lower yield stress threshold of the AA6082-T4, as compared with the AA6082-T6, was responsible for a lower compressive residual stress when the material reached the maximum temperature during the process. Such a lower value then induced a higher tensile residual stress when the material cooled down and the constrained shrinkage process occurred.

Alongside, a qualitative analysis of the weld inherent transverse distortion was performed, even though it was ancillary to the present residual stress investigation. Despite this, a distinctive

"V-like" distortion for the HYB weld of approximatively 1.4° was detected. On the other hand no significant joint distortion was observed for the FSW.

The results presented herein will definitively be helpful to develop new strategies to mitigate the presence of residual stress and thus improving the structural integrity performance of HYB welded structures.

Declaration of Competing Interest

The authors declared no conflict of interest.

Acknowledgement

L.U.P. di Bailotti (Udine, Italy) is acknowledged for performing the WEDM cuts.

The authors acknowledge the financial support from HyBond AS, Norwegian University of Science and Technology – NTNU – (Trondheim, Norway) and NAPIC (NTNU Aluminium Product Innovation Center). They are indebted to Tor Austigard of HyBond AS for valuable assistance in producing the HYB butt weld examined in the present investigation and also to Equinor ASA for carrying out the subsequent procedure testing aimed at qualifying HYB for offshore use.

The authors wish to thank Davide Bortoluzzi and Alessandra Bordon of the Laboratory for Advanced Mechatronics – LAMA FVG – (University of Udine, Italy) who carried out the CMM measurements. The authors are particularly grateful to Hexagon AB and AlmaTec S.r.l. for their beneficial cooperation with the University of Udine and their valuable contribution to the creation of LAMA's metrology room.

Professor Alex Lanzutti and Michele Magnan – Laboratorio dei Materiali Avanzati, University of Udine - are acknowledged.

Credit author statement

Alessandro Tognan: Conceptualisation, Methodology, Software, Investigation, Data Curation, Writing original draft.
Lise Sandnes: Validation, Investigation, Resources.
Giovanni Totis: Validation, Investigation.
Marco Sortino: Validation, Investigation.
Filippo Berto: Validation, Investigation, Resources.
Øystein Grong: Validation, Investigation, Resources.
Enrico Salvati: Conceptualisation, Methodology, Investigation, Writing original draft, Supervision, Funding acquisition.
All the authors have equally contributed in writing review and editing.

Appendix

Let us consider the displacement map $u_z^P(x_g, y_g)$ of the half-plate P and its cut surface Ω_P. Let us suppose that all the collected sample $1, \dots, N$ of $u_z^P(x_g, y_g)$ are arranged in the following matrix:

$$W = \begin{bmatrix} x^{(1)} & y^{(1)} & u_z^P(x_g^{(1)}, y_g^{(1)}) \\ x^{(2)} & y^{(2)} & u_z^P(x_g^{(2)}, y_g^{(2)}) \\ \vdots & \vdots & \vdots \\ x^{(N)} & y^{(N)} & u_z^P(x_g^{(N)}, y_g^{(N)}) \end{bmatrix} \in \mathbb{R}^{Nx3} \tag{7}$$

For convenience, the generic row-vector, $w^{(m)}$, of W is contracted as $w^{(m)} = \left[x^{(m)} \quad y^{(m)} \quad u_{zz}^P\left(x_g^{(m)}, y_g^{(m)}\right)\right]$, and therefore W can be written in a block-partitioned form:

$$W = [w^{(1)}|w^{(2)}|\cdots|w^{(N)}]^T$$

Suppose also that the samples $w^{(m)}$ were acquired with respect to the reference frame $\{O, x', y', z'\}$ which is not necessarily aligned with $\{O, x, y, z\}$, see Fig. 4(a). Without loss of generality, the

origins of such reference frames are supposed to be coincident. The centroid $G = [x_g \quad y_g \quad z_g]$of $u_z^P(x_g, y_g)$ is calculated and a new reference frame is defined: $\{G, x', y', z'\}$. A change of basis, i.e. a translation in this case, is necessary to express $w^{(m)}$with respect to $\{G, x', y', z'\}$, so that each $w^{(m)}$ is transformed into $w_G^{(m)}$. Therefore, the matrix W indeed transforms into:

$$W = \left[w_G^{(1)} | w_G^{(2)} | \cdots | w_G^{(N)}\right]^T$$

The Singular Value Decomposition can be immediately applied to decompose W as follows:

$$W = Q\Sigma P$$

where $Q \in \mathbb{R}^{NxN}$ and $P \in \mathbb{R}^{3x3}$ are orthonormal matrices, and $\Sigma \in \mathbb{R}^{Nx3}$ is the matrix of the so-called singular values. Finally, the following computation is performed:

$$w_{SVD}^{(m)} = P w_G^{(m)} \; \forall m \in \{1, \dots, N\} \tag{8}$$

which physically represents a rotation about the centroid *G*, given that *P* is orthonormal. As a result, W changes as:

$$W = \left[w_{SVD}^{(1)} | w_{SVD}^{(2)} | \cdots | w_{SVD}^{(N)}\right]^T \tag{9}$$

According to Eq. (7), Eq. (9) represents a new displacement map $u_{z,SVD}^P(x_g, y_g)$. The rotation in Eq. (8) allows for describing $u_z^P(x_g, y_g)$ in a new reference frame, named $\{G, x_{SVD}, y_{SVD}, z_{SVD}\}$. Intriguingly, the axes of such a reference frame, $\{x_{SVD}, y_{SVD}, z_{SVD}\}$, are aligned with the directions along those the point of the original displacement map $u_z^P(x_g, y_g)$ are distributed. In particular, x_{SVD} and y_{SVD} are (approximately) aligned with the width and the thickness of Ω_P, whereas $z_{SVD}$is (approximately) aligned with the direction of the elastic relaxation. It should be mentioned that manual reflections of $u_{z,SVD}^P(x_g, y_g)$ may be required if $det(P) = -1$. The procedure just outlined turns out to be quite useful, especially when the CMM data may not have been directly aligned with

$\{G, x_{SVD}, y_{SVD}, z_{SVD}\}$. It is worth noting, however, that minimal final adjustments might be required to achieve the optimal orientation of $u_z^P(x_g, y_g)$. Ultimately, is possible to express $u_{z,SVD}^P(x_g, y_g)$with respect to a more convenient reference, such as $\{O, x, y, z\}$ in Fig. 4(a), as far as the subsequent steps of the CM are concerned. In order to lighten the notation, $u_z^P(x_g, y_g)$ was used to indicate $u_{z,SVD}^P(x_g, y_g)$ in the present paper.

6 References

[1] W. Cai *et al.*, 'A State-of-the-Art Review on Solid-State Metal Joining', *Journal of Manufacturing Science and Engineering*, vol. 141, no. 3, p. 031012, Mar. 2019, doi: 10.1115/1.4041182.

[2] R. S. Mishra and Z. Y. Ma, 'Friction stir welding and processing', *Materials Science and Engineering: R: Reports*, vol. 50, no. 1–2, pp. 1–78, Aug. 2005, doi: 10.1016/j.mser.2005.07.001.

[3] J. S. Jesus, J. M. Costa, A. Loureiro, and J. M. Ferreira, 'Assessment of friction stir welding aluminium T-joints', *Journal of Materials Processing Technology*, vol. 255, pp. 387–399, May 2018, doi: 10.1016/j.jmatprotec.2017.12.036.

[4] D. G. Mohan and S. Gopi, 'A Review on Friction Stir Welded T-Joint', *International Journal of Science Technology & Engineering*, vol. 2, no. 07, p. 7, 2016.

[5] M. T. Milan *et al.*, 'Residual Stress Evaluation of AA2024-T3 Friction Stir Welded Joints', *J of Materi Eng and Perform*, vol. 16, no. 1, pp. 86–92, Feb. 2007, doi: 10.1007/s11665-006-9013-z.

[6] L. Śnieżek, R. Kosturek, M. Wachowski, and B. Kania, 'Microstructure and Residual Stresses of AA2519 Friction Stir Welded Joints under Different Heat Treatment Conditions', *Materials*, vol. 13, no. 4, p. 834, Feb. 2020, doi: 10.3390/ma13040834.

[7] H. Uzun, C. Dalle Donne, A. Argagnotto, T. Ghidini, and C. Gambaro, 'Friction stir welding of dissimilar Al 6013-T4 To X5CrNi18-10 stainless steel', *Materials & Design*, vol. 26, no. 1, pp. 41–46, Feb. 2005, doi: 10.1016/j.matdes.2004.04.002.

[8] A. Yazdipour and A. Heidarzadeh, 'Effect of friction stir welding on microstructure and mechanical properties of dissimilar Al 5083-H321 and 316L stainless steel alloy joints', *Journal of Alloys and Compounds*, vol. 680, pp. 595–603, Sep. 2016, doi: 10.1016/j.jallcom.2016.03.307.

[9] P. L. Threadgill, A. J. Leonard, H. R. Shercliff, and P. J. Withers, 'Friction stir welding of aluminium alloys', *International Materials Reviews*, vol. 54, no. 2, pp. 49–93, Mar. 2009, doi: 10.1179/174328009X411136.

[10] Ø. Grong, 'Recent advances in solid-state joining of aluminum', *Welding Journal*, vol. 91, no. 1, pp. 26–33, 2012.

[11] Ø. Grong, L. Sandnes, and F. Berto, 'A Status Report on the Hybrid Metal Extrusion & Bonding (HYB) Process and Its Applications', *Material Design & Processing Communications*, vol. 1, p. e41, Feb. 2019, doi: 10.1002/mdp2.41.

[12] L. Sandnes, L. Romere, F. Berto, T. Welo, and Ø. Grong, 'Assessment of the Mechanical Integrity of a 2 mm AA6060-T6 Butt Weld Produced Using the Hybrid Metal Extrusion & Bonding (HYB) Process – Part I: Bend Test Results', *Procedia Manufacturing*, vol. 34, pp. 147–153, 2019, doi: 10.1016/j.promfg.2019.06.132.

[13] L. Sandnes, L. Romere, Ø. Grong, F. Berto, and T. Welo, 'Assessment of the Mechanical Integrity of a 2 mm AA6060-T6 Butt Weld Produced Using the Hybrid Metal Extrusion & Bonding (HYB) Process – Part II: Tensile Test Results', *Procedia Structural Integrity*, vol. 17, pp. 632–642, 2019, doi: 10.1016/j.prostr.2019.08.085.

[14] L. Sandnes, Ø. Grong, T. Welo, and F. Berto, 'Fatigue properties of AA6060- T6 butt welds made by hybrid metal extrusion & bonding', *Fatigue Fract Eng Mater Struct*, vol. 43, no. 10, pp. 2349–2358, Oct. 2020, doi: 10.1111/ffe.13302.

[15] E. Salvati and A. M. Korsunsky, 'An analysis of macro- and micro-scale residual stresses of Type I, II and III using FIB-DIC micro-ring-core milling and crystal plasticity FE modelling', *International Journal of Plasticity*, vol. 98, pp. 123–138, Nov. 2017, doi: 10.1016/j.ijplas.2017.07.004.

[16] A. Greco, E. Sgambitterra, and F. Furgiuele, 'A new methodology for measuring residual stress using a modified Berkovich nano-indenter', *International Journal of Mechanical Sciences*, vol. 207, p. 106662, Oct. 2021, doi: 10.1016/j.ijmecsci.2021.106662.

[17] M. N. James, 'Residual stress influences on structural reliability', *Engineering Failure Analysis*, vol. 18, no. 8, pp. 1909–1920, Dec. 2011, doi: 10.1016/j.engfailanal.2011.06.005.

[18] E. Salvati, H. Zhang, K. S. Fong, X. Song, and A. M. Korsunsky, 'Separating plasticity-induced closure and residual stress contributions to fatigue crack retardation following an overload', *Journal of the Mechanics and Physics of Solids*, vol. 98, pp. 222–235, Jan. 2017, doi: 10.1016/j.jmps.2016.10.001.

[19] M. Benedetti, V. Fontanari, C. Santus, and M. Bandini, 'Notch fatigue behaviour of shot peened high-strength aluminium alloys: Experiments and predictions using a critical distance method', *International Journal of Fatigue*, vol. 32, no. 10, pp. 1600–1611, Oct. 2010, doi: 10.1016/j.ijfatigue.2010.02.012.

[20] J. Everaerts, E. Salvati, F. Uzun, L. Romano Brandt, H. Zhang, and A. M. Korsunsky, 'Separating macro- (Type I) and micro- (Type II+III) residual stresses by ring-core FIB-DIC milling and eigenstrain modelling of a plastically bent titanium alloy bar', *Acta Materialia*, vol. 156, pp. 43–51, Sep. 2018, doi: 10.1016/j.actamat.2018.06.035.

[21] M. N. James *et al.*, 'Residual stresses and fatigue performance', *Engineering Failure Analysis*, vol. 14, no. 2, pp. 384–395, Mar. 2007, doi: 10.1016/j.engfailanal.2006.02.011.

[22] P. J. Withers, 'Residual stress and its role in failure', *Rep. Prog. Phys.*, vol. 70, no. 12, pp. 2211–2264, Dec. 2007, doi: 10.1088/0034-4885/70/12/R04.

[23] N. S. M. Nasir, 'REVIEW ON WELDING RESIDUAL STRESS', *ARPN Journal of Engineering and Applied Sciences*, vol. 11, no. 9, p. 10, 2016.

[24] F. Uzun and A. M. Korsunsky, 'On the identification of eigenstrain sources of welding residual stress in bead-on-plate inconel 740H specimens', *International Journal of Mechanical Sciences*, vol. 145, pp. 231–245, Sep. 2018, doi: 10.1016/j.ijmecsci.2018.07.007.

[25] A. Kouadri-Henni, C. Seang, B. Malard, and V. Klosek, 'Residual stresses induced by laser welding process in the case of a dual-phase steel DP600: Simulation and experimental approaches', *Materials & Design*, vol. 123, pp. 89–102, Jun. 2017, doi: 10.1016/j.matdes.2017.03.022.

[26] J. R. Chukkan, G. Wu, M. E. Fitzpatrick, S. Jones, and J. Kelleher, 'An iterative technique for the reconstruction of residual stress fields in a butt-welded plate from experimental measurement, and comparison with welding process simulation', *International Journal of Mechanical Sciences*, vol. 160, pp. 421–428, Sep. 2019, doi: 10.1016/j.ijmecsci.2019.07.001.

[27] H. Jamshidi Aval, 'Microstructure and residual stress distributions in friction stir welding of dissimilar aluminium alloys', *Materials & Design*, vol. 87, pp. 405–413, Dec. 2015, doi: 10.1016/j.matdes.2015.08.050.

[28] M. Peel, A. Steuwer, M. Preuss, and P. J. Withers, 'Microstructure, mechanical properties and residual stresses as a function of welding speed in aluminium AA5083 friction stir welds', *Acta Materialia*, vol. 51, no. 16, pp. 4791–4801, Sep. 2003, doi: 10.1016/S1359-6454(03)00319-7.

[29] E. Salvati, J. Everaerts, K. Kageyama, and A. M. Korsunsky, 'Transverse fatigue behaviour and residual stress analyses of double sided FSW aluminium alloy joints', *Fatigue Fract Eng Mater Struct*, vol. 42, no. 9, pp. 1980–1990, Sep. 2019, doi: 10.1111/ffe.13068.

[30] T.-S. Jun, K. Dragnevski, and A. M. Korsunsky, 'Microstructure, residual strain, and eigenstrain analysis of dissimilar friction stir welds', *Materials & Design*, vol. 31, pp. S121–S125, Jun. 2010, doi: 10.1016/j.matdes.2009.11.042.

[31] A. P. Reynolds, W. Tang, T. Gnaupel-Herold, and H. Prask, 'Structure, properties, and residual stress of 304L stainless steel friction stir welds', *Scripta Materialia*, vol. 48, no. 9, pp. 1289–1294, May 2003, doi: 10.1016/S1359-6462(03)00024-1.

[32] M. Haghshenas, M. A. Gharghouri, V. Bhakhri, R. J. Klassen, and A. P. Gerlich, 'Assessing residual stresses in friction stir welding: neutron diffraction and nanoindentation methods', *Int J Adv Manuf Technol*, vol. 93, no. 9–12, pp. 3733–3747, Dec. 2017, doi: 10.1007/s00170-017-0759-2.

[33] M. Bhattacharyya, 'Evaluation of residual stresses in isothermal friction stir welded 304L stainless steel plates', *Materials Science and Engineering: A*, p. 39, 2021.

[34] M. Prime, 'Cross-Sectional Mapping of Residual Stresses by Measuring the Surface Contour After a Cut', *Journal of Engineering Materials and Technology*, vol. 123, pp. 162–168, May 2001, doi: 10.1115/1.1345526.

[35] M. Prime, T. Gnäupel-Herold, J. Baumann, R. Lederich, D. Bowden, and R. Sebring, 'Residual stress measurements in a thick, dissimilar aluminum alloy friction stir weld', *Acta Materialia*, vol. 54, pp. 4013–4021, Jan. 2006, doi: 10.1016/j.actamat.2006.04.034.

[36] C. Liu and X. Yi, 'Residual stress measurement on AA6061-T6 aluminum alloy friction stir butt welds using contour method', *Materials & Design*, vol. 46, pp. 366–371, Apr. 2013, doi: 10.1016/j.matdes.2012.10.030.

[37] P. Carlone and G. S. Palazzo, 'Longitudinal Residual Stress Analysis in AA2024-T3 Friction Stir Welding', *TOMEJ*, vol. 7, no. 1, pp. 18–26, Aug. 2013, doi: 10.2174/1874155X01307010018.

[38] C. Zhang and A. A. Shirzadi, 'Measurement of residual stresses in dissimilar friction stir-welded aluminium and copper plates using the contour method', *Science and Technology of Welding and Joining*, vol. 23, no. 5, pp. 394–399, Jul. 2018, doi: 10.1080/13621718.2017.1402846.

[39] H. Jafari, H. Mansouri, and M. Honarpisheh, 'Investigation of residual stress distribution of dissimilar Al-7075-T6 and Al-6061-T6 in the friction stir welding process strengthened with SiO2 nanoparticles', *Journal of Manufacturing Processes*, vol. 43, pp. 145–153, Jul. 2019, doi: 10.1016/j.jmapro.2019.05.023.

[40] I. Alinaghian, S. Amini, and M. Honarpisheh, 'Residual stress, tensile strength, and macrostructure investigations on ultrasonic assisted friction stir welding of AA 6061-T6', *The Journal of Strain Analysis for Engineering Design*, vol. 53, no. 7, pp. 494–503, Oct. 2018, doi: 10.1177/0309324718789768.

[41] I. Alinaghian, M. Honarpisheh, and S. Amini, 'The influence of bending mode ultrasonic-assisted friction stir welding of Al-6061-T6 alloy on residual stress, welding force and macrostructure', *Int J Adv Manuf Technol*, vol. 95, no. 5–8, pp. 2757–2766, Mar. 2018, doi: 10.1007/s00170-017-1431-6.

[42] S. Sunny, R. Mathews, G. Gleason, A. Malik, and J. Halley, 'Effect of metal additive manufacturing residual stress on post-process machining-induced stress and distortion', *International Journal of Mechanical Sciences*, vol. 202–203, p. 106534, Jul. 2021, doi: 10.1016/j.ijmecsci.2021.106534.

[43] R. Mathews, S. Sunny, A. Malik, and J. Halley, 'Coupling between inherent and machining-induced residual stresses in aluminum components', *International Journal of Mechanical Sciences*, p. 106865, Oct. 2021, doi: 10.1016/j.ijmecsci.2021.106865.

[44] D. Yan, A. Wu, J. Silvanus, and Q. Shi, 'Predicting residual distortion of aluminum alloy stiffened sheet after friction stir welding by numerical simulation', *Materials & Design*, vol. 32, no. 4, pp. 2284–2291, Apr. 2011, doi: 10.1016/j.matdes.2010.11.032.

[45] W. He, J. Liu, W. Hu, G. Wang, and W. Chen, 'Controlling residual stress and distortion of friction stir welding joint by external stationary shoulder', *High Temperature Materials and Processes*, vol. 38, no. 2019, pp. 662–671, Feb. 2019, doi: 10.1515/htmp-2019-0005.

[46] W. Woo, H. Choo, D. W. Brown, Z. Feng, and P. K. Liaw, 'Angular distortion and through-thickness residual stress distribution in the friction-stir processed 6061-T6 aluminum alloy', *Materials Science and Engineering: A*, vol. 437, no. 1, pp. 64–69, Nov. 2006, doi: 10.1016/j.msea.2006.04.066.

[47] L. Sandnes, G. Rørvik, I. Kulbotten, Ø. Grong, and F. Berto, 'Qualification of the Hybrid Metal Extrusion & Bonding (HYB) Process for Welding of Aluminium Offshore Structures', *Material Design & Processing Communications*, Jun. 2020, doi: 10.1002/mdp2.194.

[48] F. Leoni, Ø. Grong, L. Sandnes, and F. Berto, 'High temperature tensile properties of AA6082 filler wire used for solid-state joining', *Procedia Structural Integrity*, vol. 25, pp. 348–354, 2020, doi: 10.1016/j.prostr.2020.04.039.

[49] H. Ma, Q. Hou, Z. Yu, and P. Ni, 'Stability of 6082-T6 aluminum alloy columns under axial forces at high temperatures', *Thin-Walled Structures*, vol. 157, p. 107083, Dec. 2020, doi: 10.1016/j.tws.2020.107083.

[50] X. Guo, L. Tao, S. Zhu, and S. Zong, 'Experimental Investigation of Mechanical Properties of Aluminum Alloy at High and Low Temperatures', *J. Mater. Civ. Eng.*, vol. 32, no. 2, p. 06019016, Feb. 2020, doi: 10.1061/(ASCE)MT.1943-5533.0003002.

[51] N. K. Langhelle and J. Amdahl, 'Experimental and Numerical Analysis of Aluminium Columns Subjected to Fire', *The International Society of Offshore and Polar Engineers*, 2001.

[52] O. R. Myhr, Ø. Grong, and C. Schäfer, 'An Extended Age-Hardening Model for Al-Mg-Si Alloys Incorporating the Room-Temperature Storage and Cold Deformation Process Stages', *Metall and Mat Trans A*, vol. 46, no. 12, pp. 6018–6039, Dec. 2015, doi: 10.1007/s11661-015-3175-y.

[53] F. Hosseinzadeh, P. Bouchard, and J. Kowal, 'Towards good practice guidelines for the contour method of residual stress measurement', *Journal of Engineering*, vol. 2014, Jul. 2014, doi: 10.1049/joe.2014.0134.

[54] E. Salvati and A. M. Korsunsky, 'Micro-scale measurement & FEM modelling of residual stresses in AA6082-T6 Al alloy generated by wire EDM cutting', *Journal of Materials Processing Technology*, vol. 275, p. 116373, Jan. 2020, doi: 10.1016/j.jmatprotec.2019.116373.

[55] N. Naveed, 'Guidelines to select suitable parameters for contour method stress measurements', *Archives of Mechanics*, vol. 72, no. 1, Art. no. 1, Feb. 2020, doi: 10.24423/aom.3378.

[56] M. J. Roy, N. Stoyanov, R. J. Moat, and P. J. Withers, 'pyCM: An open-source computational framework for residual stress analysis employing the Contour Method', *SoftwareX*, vol. 11, p. 100458, Jan. 2020, doi: 10.1016/j.softx.2020.100458.

[57] C. Geuzaine and J.-F. Remacle, 'Gmsh: A 3-D finite element mesh generator with built-in pre- and post-processing facilities', *International Journal for Numerical Methods in Engineering*, vol. 79, no. 11, pp. 1309–1331, 2009, doi: https://doi.org/10.1002/nme.2579.

[58] M. B. Toparli and M. E. Fitzpatrick, 'Development and Application of the Contour Method to Determine the Residual Stresses in Thin Laser-Peened Aluminium Alloy Plates', *Exp Mech*, vol. 56, no. 2, pp. 323–330, Feb. 2016, doi: 10.1007/s11340-015-0100-7.

[59] M. D. Olson, A. T. DeWald, M. B. Prime, and M. R. Hill, 'Estimation of Uncertainty for Contour Method Residual Stress Measurements', *Exp Mech*, vol. 55, no. 3, pp. 577–585, Mar. 2015, doi: 10.1007/s11340-014-9971-2.

[60] S. W. Williams and A. Steuwer, 'Residual stresses in friction stir welding', in *Friction Stir Welding*, Elsevier, 2010, pp. 215–244. doi: 10.1533/9781845697716.2.215.

[61] F. Leoni, Ø. Grong, L. Sandnes, T. Welo, and F. Berto, 'Finite element modelling of the filler wire feeding in the hybrid metal extrusion & bonding (HYB) process', *Journal of Advanced Joining Processes*, vol. 1, p. 100006, Mar. 2020, doi: 10.1016/j.jajp.2020.100006.

[62] L. Sandnes, Ø. Grong, J. Torgersen, T. Welo, and F. Berto, 'Exploring the hybrid metal extrusion and bonding process for butt welding of Al–Mg–Si alloys', *Int J Adv Manuf Technol*, vol. 98, no. 5–8, pp. 1059–1065, Sep. 2018, doi: 10.1007/s00170-018-2234-0.

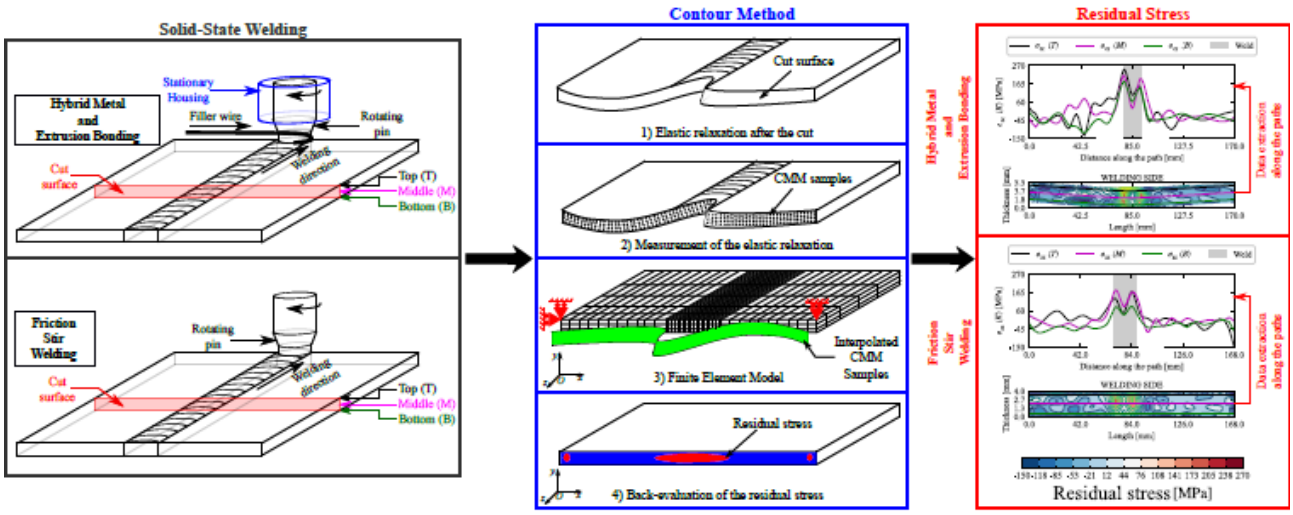

Graphical